POLITECNICO
MILANO 1863

DIPARTIMENTO DI MECCANICA

mecc

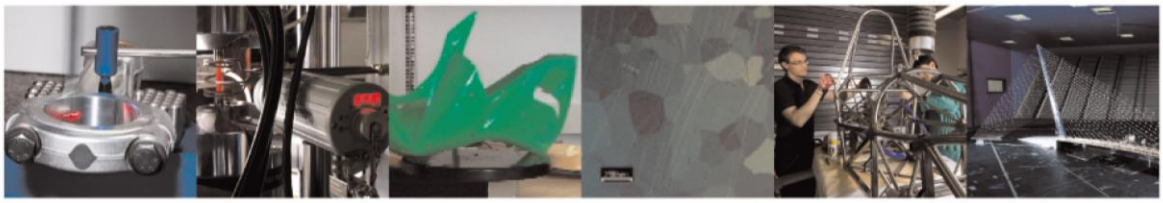

Understanding the deformation mechanisms of horizontal internal channels during the LPBF of 18Ni300 maraging steel

Fabio Belloli, Ali Gökhan Demir, Barbara Previtali

This is a post-peer-review, pre-copyedit version of an article published in Journal of Manufacturing Processes. The final authenticated version is available online at: http://dx.doi.org/10.1016/j.jmapro.2021.07.063

DIPARTIMENTO DI MECCANICA ■ POLITECNICO DI MILANO
via G. La Masa, 1 ■ 20156 Milano ■ EMAIL (PEC): pecmecc@cert.polimi.it
http://www.mecc.polimi.it
Rev. 0

Understanding the deformation mechanisms of horizontal internal channels during the LPBF of 18Ni300 maraging steel

Fabio Belloli, Ali Gökhan Demir*, Barbara Previtali

Department of Mechanical Engineering, Politecnico di Milano, Via La Masa 1, 20156 Milan, Italy

*Corresponding author: aligokhan.demir@polimi.it

Understanding the deformation mechanisms of horizontal internal channels during the LPBF of 18Ni300 maraging steel

Fabio Belloli, Ali Gökhan Demir*, Barbara Previtali

Department of Mechanical Engineering, Politecnico di Milano, Via La Masa 1, 20156 Milan, Italy

*Corresponding author: aligokhan.demir@polimi.it

Abstract

The 18Ni300 maraging steel is arguably the standard material for mould and die production employing laser powder bed fusion (LPBF). Owing to its good processability via the LPBF process and high strength after the aging treatment, 18Ni300 maraging steel has been widely employed for producing complex moulds with internal conformal channels. In order to fully take advantage of the cooling channels within the mould, these channels should respect the geometrical and dimensional requirements. An apparent issue concerning the internal channels is the geometrical deformations occurring during the process. With other alloys used in LPBF such as stainless steel, the circular horizontal holes tend to deform in tension around the upper arch, resulting in hole enlargement around this region. However, the 18Ni300 is highly sensitive to the thermal history during the LPBF process and can deform differently according to the channel geometry. The use of supports in horizontal channels as a remedy is not suitable due to the difficulty of their removal. Alternatively, the use of non-circular profiles may act as stress accumulation zones during the lifetime of the die. Accordingly, this work studies the deformation mechanisms during the LPBF 18Ni300 maraging steel concerning two types of channel profiles, namely circular and diamond shaped. Samples with different channel widths and lengths were produced and geometrical deviations were measured. Powder bed monitoring data and microstructural analyses were made to construct a phenomenological description of the deformation mechanism. The results indicate that the final form of the channel depends also on the thermal history of the successive layer once the horizontal channel is closed. The influence of volumetric expansion in martensitic transformation was found to be relevant on the generation of an apparent compression field. An analytical model was used to estimate an equivalent stress value starting from the experimental data showing a compression state. The results confirmed that the 18Ni300 deformation depends on the channel form and dimensions, moreover occurs differently compared to other LPBF alloys such as stainless steels, Al-, Ni-, and Ti- alloys, which deform outward in a tension state.

Keywords: Additive manufacturing; laser powder bed fusion; phase transformation induced deformation; part deformation; mould making

1 Introduction

Laser powder bed fusion (LPBF) has opened up several possibilities in tool and mould making with several application fields such as automotive, aerospace, and consumer products. The geometrical flexibility provided by this additive manufacturing (AM) technique allows for producing high performance moulds with better lubrification and cooling properties [1]. A key feature of LPBF is the

possibility to obtain conformal cooling channels in the complex mould shapes. The conformal channels can ease the heating and cooling cycles in injection moulding dies for instance [2]. Despite such advantages, for a broader use of the AM technology in mould making, several aspects require attention. The feasibility of producing these intricate internal channels with the required geometrical fidelity remains an important issue. Indeed, design [3], manufacturing, finishing [4], and inspection [5] of the internal channels produced by LPBF require a different way of reasoning compared to the conventional mould manufacturing.

In LPBF, several design rules exist in order to provide the feasibility of producing the desired product. Such rules regard the extension of overhang regions, part orientation and the inclination of the produced walls with respect to the build platform plane [6,7]. Despite being one of the simplest forms to be produced, the generation of a circular channel requires attention [8]. Commonly the horizontal circular holes tend to curl upwards around the upper arch [9][10], which is due to the thermal stresses generated during the build [11]. As a generic rule horizontal circular channels require supporting on the upper arch, when the diameter exceeds 10 mm. Support structures can help resolve the channel deformation issue, while for long and complex geometries their removal becomes a very complicated task. A common consideration is to redesign the channel geometry similar to a teardrop to avoid acute angle formations on the upper arch [3]. The teardrop shape can overcome the geometrical deviations from the nominal shape. However, the sharp corners are stress accumulating zones and can be prone to crack formation. The modification of process parameters to compensate the deformations through a priori modelling has been proposed as a solution [12]. Another approach regards the modelling of the deformation mechanism and compensating the geometrical deviation at the level of the digital model [13]. Recently, commercial codes have been made available to the end-users for compensating part deformations especially concerning the large components [14][15]. The deformation characteristics of internal channels have received relative less attention from this point of view. On a future prospect, the use of online closed loop control strategies can also overcome such deformations in the overhang regions [16][17].

The extent of the geometrical distortions in LPBF is related to the thermal field induced by the process parameters such as the laser power, scan speed, layer thickness, hatching distance and rotation [18], but also the scan strategy [19–21] and the preheating [22,23] used in the process. The influence of the processed material is intrinsic but requires more attention from the scientific literature. For tool and mould making several steel grades are available commercially such as the AISI 316 austenitic stainless steel [24], 17-4 PH precipitation hardening stainless steel [25], 15-5 precipitation hardening martensitic stainless steel [26], H13 hot work tool steel [2], and 18Ni300 maraging steel. All these alloys provide specific advantages where the 18Ni300 maraging steel has been proven to be the primary solution as it provides superior mechanical properties and high wear resistance after the designated heat treatment.

The 18Ni300 belongs to a class of iron-nickel steels featured by a very low content of carbon [27]. They are characterized by a lath martensite matrix hardened by the precipitation of intermetallic compounds after an ageing heat treatment. A peculiarity of the martensite transformation in these steels is that it happens independently from the cooling rate. The precipitation occurs during the ageing treatment, that consists in heating the material to 450-510°C for 3 to 9h. Excessive holding duration can result in the reversion of the martensitic matrix to austenite, which can also be exploited to improve toughness [28]. Usually, to favour the precipitation hardening, a solubilization is done before the ageing. The solubilization is a heat treatment done typically at 815°C for 1h every 25 mm of thickness to homogenizes microstructure of the component inherited from previous treatments and to control the final microstructure by controlling the cooling rate and to place the alloying elements in solid solution before cooling.

The properties of the 18Ni300 maraging steel render it the principal material choice for additively manufacturing dies and moulds for especially for injection moulding and die casting applications.

Amongst the conventional alloys used in LPBF, the 18Ni300 provides higher strength upon the dedicated heat treatment, adequate resistance to corrosion and cyclic heating and cooling with good processability rendering it preferable over other alloys such as AISI 316, H13, and 17-4PH [29]. With LPBF high performance dies and moulds can be produced with internal channels using 18Ni300 [30]. In injection moulding of polymers and die casting of low melting point alloys (eg. Al-alloys), the conformal channels allow the die to be cooled down after the injection process quickly reducing the time required for solidification. Hence, the overall cycle time for the production can be reduced. Moreover, the conformal cooling allows to reduce overheating in the zones where conventional cooling channels cannot reach. Hence, higher material temperatures could be used and injection moulded or die cast products with thin to thick section variations could be produced with greater ease. The greater control over the temperature among the mould would also allow to employ materials with lower flowability in a similar fashion. Another benefit of the greater thermal control is the he reduction of shrinkage porosity [31]. The faster cooling phase can reduce the porosity formed due to the interdentritic porosity formed at slow cooling rates observed in Al-Si alloys for instance [32]. Within the lifetime of the single die the heating and cooling cycles reach several hundreds of thousands for injection moulding and several tens of thousands for die casting. The cyclic heating and cooling renders the internal channels susceptible cracking due to thermal fatigue. The cooling channel profile should be conformal also to the mechanical resistance requirements avoiding sharp edges. Hence, the geometrical integrity of the internal channels is of paramount interest.

The processability of the 18Ni300 maraging steel has been widely studied in the literature concerning its processability via LPBF. Continuous wave (CW) emission has been principally employed in the presented works [33–35]. LPBF systems operating with pulsed wave (PW) emission have been found also effective to produce fully dense components [36,37]. Several works depict specific heat treatments for improving or even tailoring the mechanical properties [38–40]. It can be expected that the microstructure of the LPBF produced 18Ni300 can greatly differ from the conventionally manufactured alloy. The alloy is highly sensitive the thermal history, which indicates high sensitivity also to the process parameters, the platform preheating and the scan strategy [41–43]. Indeed, the response to the heat treatment stages can also change depending on the initial microstructure resulting from the LPBF process [44]. These factors indicate that 18Ni300 can exhibit peculiar stress fields when processed by LPBF. Despite the wide use of this alloy in mould and die production, to the authors' knowledge a comprehensive study concerning the geometrical deviations of horizontal channels has not been previously carried out.

On the other hand, several works have studied the deformation behaviour of holes, overhang regions and internal channels in LPBF. An outward deformation of the upper arch of horizontal holes due to the tension field were observed for some of the most common alloys used in LPBF such as AISI 316L [9], 17-PH [13], and IN718 [45]. This behaviour was explained by the formation of an overall tension field bending the two free ends of the arch outwards [13]. Such tension field was also verified through cantilever geometries on AlSi10Mg [23] and Ti6Al4V [46]. Recently, Bugatti and Semeraro showed that the bending behaviour of cantilever geometries produced in 18Ni300 with an LPBF system using pulsed wave laser and no platform preheating can result in negative (inward) deformation indicating a compressive stress field [47].

Accordingly, this work aims to carry out a comprehensive study on the geometrical deviations generated in circular and diamond shaped horizontal channel profiles produced by LPBF in 18Ni300 maraging steel. In particular, a systematic experimental study was carried out to quantify the geometrical deviations. The analyses were assisted with powder bed monitoring images and microstructural analysis to construct a phenomenological model. The results confirm that the channel geometry plays a marked role on the material's microstructural evolution. The resultant partial channel closure differs from other

conventional LPBF materials and was attributed to the local microstructural changes occurring on the successive layers and leading to a volume expansion. An existing analytical model proposed by Kamat and Pei [13] was used inversely to estimate an equivalent stress field. Unlike the other LPBF steels used in the fabrication of dies and tools that show a positive equivalent stress (tensile stress), horizontal circular channels built without supports in 18Ni300 reveal an unexpected behaviour with negative equivalent stress (compressive stress). The work aims to provide insights to the the deformation mechanism of horizontal internal and indications towards the corrective actions in the design step.

2 Materials and methods

2.1 Material

The powder utilized in this work was a gas atomized powder of 18Ni300 Maraging steel (Trumpf, Ditzingen, Germany). The powder size ranged between 15-45 µm and the powder morphology is shown in Figure 1. The material nominal chemical composition and measured one through EDX are reported in Table 1.

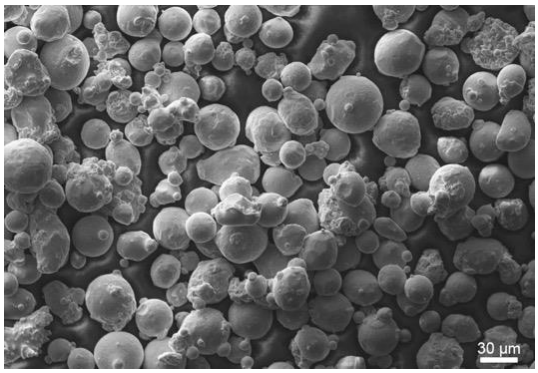

Figure 1. SEM image of the powder used in the experiments.

Table 1. Nominal and measured chemical composition of the 18Ni300 maraging steel powder (wt%).

Element	Ni	Co	Mo	Ti	Fe
Nominal	18-19	8.5-9.5	4.6-5.2	0.5-0.8	Bal.
Measured	16.9 ±0.4	9.5±0.2	5.0±0.3	0.8±0.2	67.9±0.9

2.2 LBPF system

The employed LPBF system was a Trumpf TruPrint 3000 (Ditzingen, Germany). The system employs a single mode fibre laser (RedPower Qube, SPI, Southampton, UK). The laser runs in continuous wave (CW) emission mode with a 450 W power reaching the powder bed. The optical system is composed by a 3-axis deflection system. In this system, the laser output is connected to a collimating unit. The collimated beam is launched into the zoom optics, where a moving lens compensates the focus position before a focusing lens. After passing through the focusing lens, the beam is deflected by two galvanometric mirrors. The system therefore compensates the curvature of the focusing plane and moves the beam position relatively to the powder bed. The nominal minimum beam diameter in this configuration is 100 µm. The build platform is cylindrical with 300 mm diameter and 400 mm build height. Build plate preheating could be carried out up to 200°C. Prior to the build the chamber is flooded with N_2 and the O_2 content is kept under 3000 ppm. The machine is equipped with a powder bed

monitoring system, which takes powder bed images before and after the scanning of each layer. The position of the camera and the illuminating lights are shown in Figure 2. The main characteristics of the system are reported in Table 2.

Table 2. Tumpf TruPrint 3000 main features.

Parameter	Value
Maximum laser power, P_{max}	500 W
Minimum beam diameter, d_0	100 µm
Build volume	ø300 mm x 400 mm
Platform preheating	up to 200°C

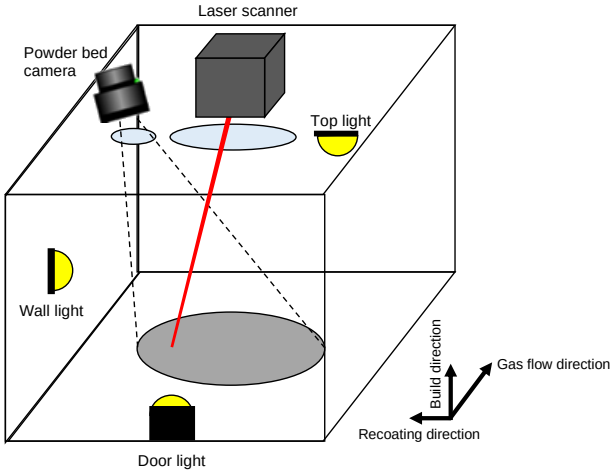

Figure 2. Schematic representation of the powder bed monitoring system.

2.3 Characterization equipment

The mechanical properties of the material were tested using a tensile test machine (MTS Alliance). The specimen geometry was prepared according to ISO-6892-1. Specimens were tested without any surface polishing. The deformation of the cooling channels was determined acquiring the 2D profile with an optical microscope (Mitutoyo Quick Vision ELF QV-202, Kanagawa, Japan). The image of the profile was then analysed by a Matlab routine, applying first binarization and then profile extraction through edge detection.

3 Experimental plan

3.1 Mechanical properties

The mechanical properties of 18Ni300 maraging steel has been shown to be susceptible to the processing conditions as seen in literature. Hence, it was required to assess the experimental conditions compared to the mechanical properties reported in literature. Tensile specimens were prepared employing the process parameters providing an apparent density above 99.5%. The tensile specimens were oriented vertically on the build plate. Three replications were tested in as-built condition and three others were tested after an aging heat treatment. A direct ageing treatment was employed, which consisted in the maintenance of the samples at 490°C for 6 hours, followed by an air cooling to room temperature.

Table 3. Process parameters used for studying the mechanical properties.

Fixed parameters	
Parameter	**Level**
Laser Power, *P* (W)	275
Hatch Distance, *h* (µm)	90
Layer Thickness, *z* (µm)	50
Scan speed, *v* (mm/s)	1000
Build plate preheating (°C)	200
Scan Strategy	Meander
Variable parameters	
Parameter	**Levels**
Heat Treatment	None, Aging

3.2 Horizontal channel deformation

The deformation analysis was carried out on samples specifically designed to simulate the production of the horizontal cooling channels. Different geometries were produced without any support structures using the same process parameters employed for the tensile specimens. The images of the powder bed monitoring system were also collected to clarify the deformations occurring during the process. Two different channel geometries were selected namely circular and diamond shaped. For each geometry the characteristic dimension (the diameter for the circular channels and the slope of the wall for the diamond shaped channels) was varied together with the thickness. The experimental conditions are summarized in Table 4.

Table 4. Design of the Experiment of cooling channel deformation.

Fixed parameters			
Factor		**Level**	
Laser Power, *P* (W)		275	
Hatch Distance, *h* (µm)		90	
Layer Thickness, *z* (µm)		50	
Scan speed, *v* (mm/s)		1200	
Build plate preheating (°C)		200	
Scan strategy		Meander	
Varied parameters			
Circular Channel		**Diamond Shaped Channel**	
Parameter	**Levels**	Parameters	**Levels**
Diameter, *D* (mm)	5 – 7.5 – 10	Wall Inclination, φ (°)	45 – 50
Thickness, *b* (mm)	10 – 15 – 20	Thickness, *b* (mm)	10 – 15 – 20

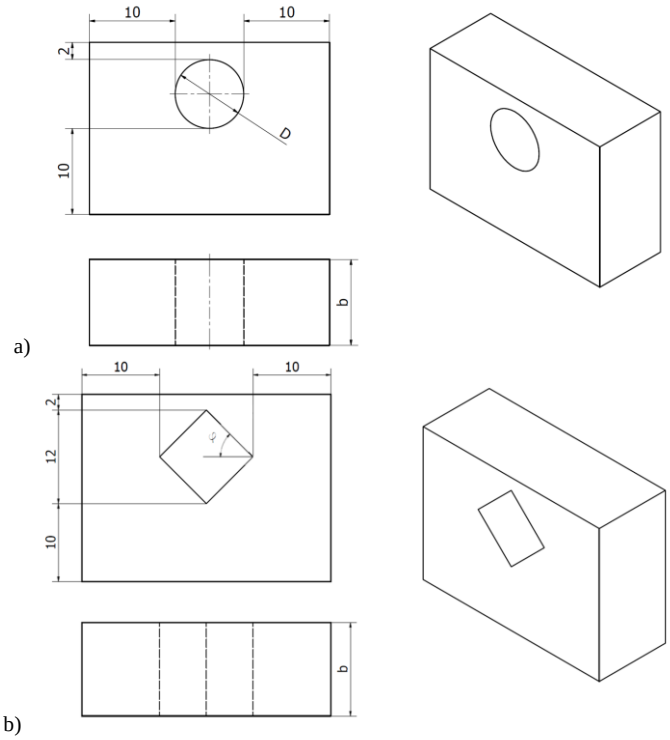

Figure 3. a) Circular and b) diamond shaped channel geometry.

Figure 3 shows the designed channel geometries. The samples were designed so that the channel geometry grows with the same surrounding conditions: 10 mm from the sides and the bottom and 2 mm from the top. In particular, the sidewalls were designed so that the overhanging is built as a cantilever clamped to one end. Each condition was replicated three times for a total of 45 specimens. Supports were placed under each sample in order to facilitate the removal from the base plate. Standard rectangular supports were employed with 2 mm x 0.5 mm section and tooth shaped connection to the built specimens. The size of the specimens allowed avoiding the influence of the support structures on the deformation of the horizontal channels as they were sufficiently far from the bottom side of channels (10 mm).

The analysis of the deformation was carried out separately for the two analysed geometries, but in a similar way. Firstly, the difference between the measured profile and nominal were quantified. Deformation profiles are modelled using the average yield stress of as built material. The first step to analyse the deformation of the measured profile was to find the centre of it. The lower part of the profile, considered non-deformed, was fitted with the nominal lower profile by minimizing the total sum of squares of the errors.

The analysis on the circular channels was initially performed evaluating the difference in radial direction between the nominal and the real profile, as in equation 1, with respect to a polar reference system centred in the centre of the channel (see Figure 4.a).

$$\Delta R(\theta) = R(\theta) - r \qquad 1$$

where, $\Delta R(\theta)$ is the difference between the nominal profile and the measured one in radial direction, $R(\theta)$ is the radial coordinate of the measured profile and r is the nominal radius of the profile. To have a quantitative factor to compare the deformation of the various profiles, the upper arch of each channel was fitted with an ellipse and then the vertical semi-axis of each ellipse was used as indicator of the

deviation from the designed channel of each sample. The fitting ellipse was chosen by fixing the horizontal semi-axis equal to the radius of the channel and varying the vertical one (*e* in Figure 4.a). The deflection occurred for the different channel diameters was measured finally in terms of percentage difference between the vertical semi-axis of the fitted ellipse and the radius of the designed profile. This parameter, called *normalized deviation* $D_n\%$ is calculated as in equation 2:

$$Dn\% = \frac{e - r}{r} * 100 \qquad 2$$

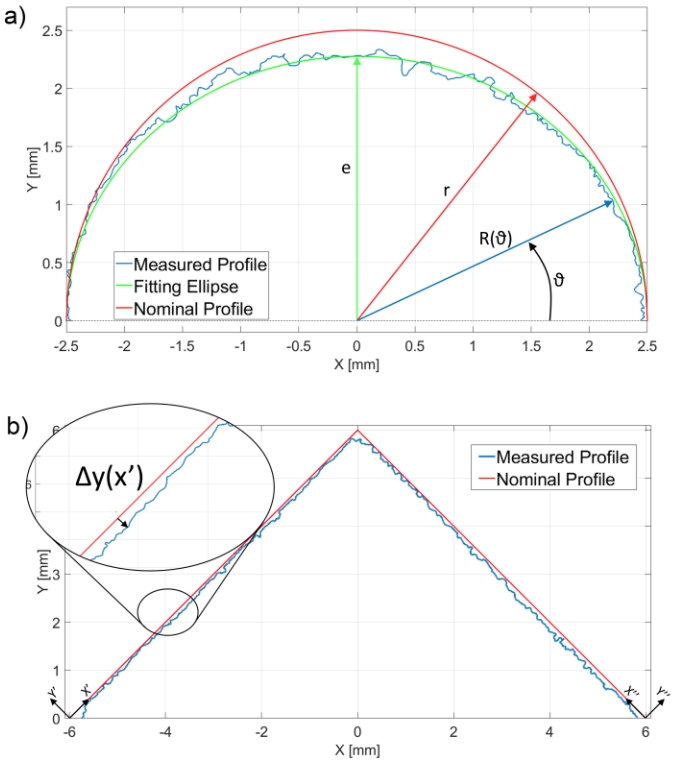

Figure 4. Scheme of the measurement method for a) circular and b) diamond shaped channels.

The analysis of the diamond shaped channels was performed considering the average distance between the nominal and the measured profile, calculated as the actual average of the distance between the two profiles (*Da*). This analysis was performed on both the walls of the channel separately (i.e. left and right) and then the two were compared to see if any difference exists. The distance of each wall profile from the nominal profile was calculated referring to a reference system centred on the bottom corner of each wall and oriented as the nominal wall (see Figure 4.b).

4 Results

4.1 Mechanical strength

Figure 5 shows typical tensile curves of the specimens in as-built and aged conditions. Table 5 summarizes the extracted mechanical properties. In Figure 6 the mechanical properties achieved are compared to the samples produced without preheating and another LPBF system operating with pulsed wave emission [40]. It should be noted that the results are not completely comparable due to several

differences in the employed LPBF systems. However, the use of preheating and a continuous wave (CW) laser appears to provide better ductility with lower UTS. The effect of increased ductility with preheating in as-built conditions has been shown previously [42]. The CW emission has also been shown to induce a larger melt pool and potentially slower cooling rates [48,49]. Along with providing the material properties required for the modelling phase, these results confirm the heat sensitivity of the material observable in a global scale.

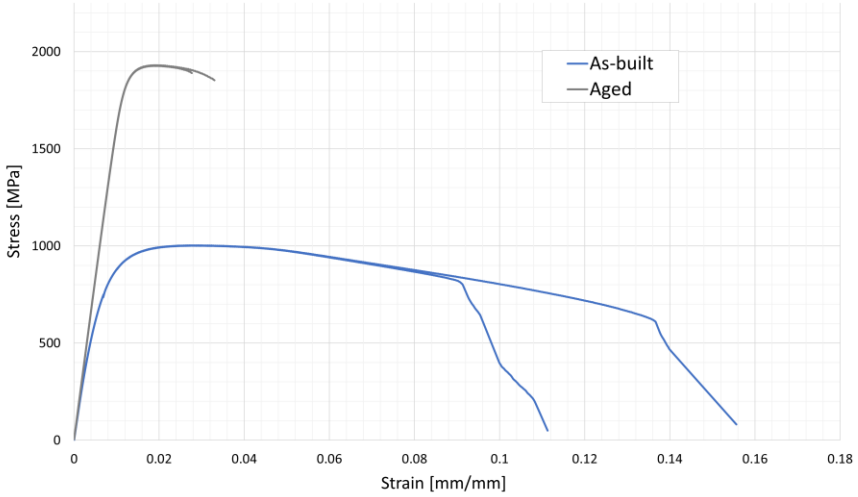

Figure 5. Stress-strain curves before and after the heat treatment.

Table 5. Mechanical properties of the as-built and aged specimens.

Parameter	As-built	Aged
Elastic modulus, E [GPa]	148±0.6	164±1.7
Yield strength, YS [MPa]	757±3.5	1876±5
Ultimate tensile strength,UTS [MPa]	1003±1	1929±1
Elongation at break, ε [%]	12.4±1.6	3.1±0.3

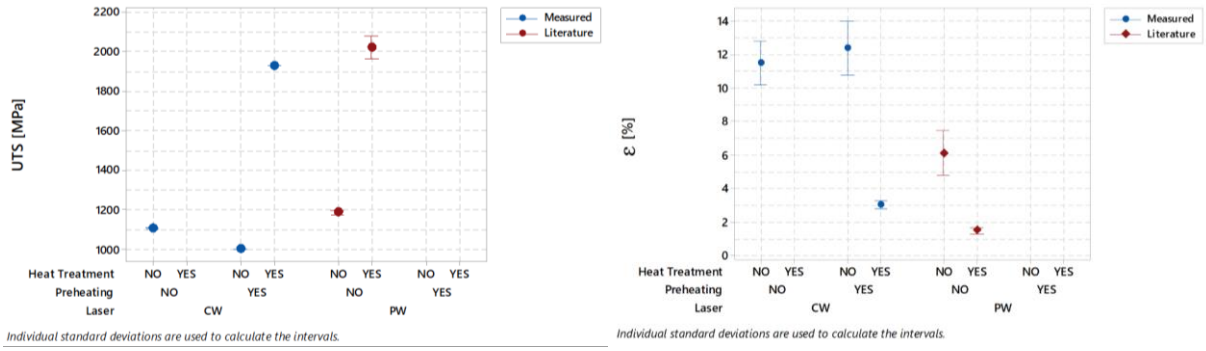

Figure 6. Influence of the heat treatment, preheating and laser emission profile on UTS and ε of 18Ni300. Literature values are extracted from [40].

4.2 Deformation behaviour of the horizontal channels

Figure 7 shows the build plate with the specimens. It can be noticed the specimens were positioned randomly, while they were rotated by 45° around the z axis in order to reduce the coating wear. Specimens were removed from the plate and cleaned to remove the excess powder. No sand-blasting was applied to reduce the surface roughness. All horizontal channels were produced without any issues concerning the overhang regions around the downskin regions. The channel dimensions were appropriately chosen with diameters not exceeding 10 mm in the circular case and with build angles higher than 45° in the case of diamond shaped channels. Hence, the support structures could be avoided and the channels did not show signs of sagging.

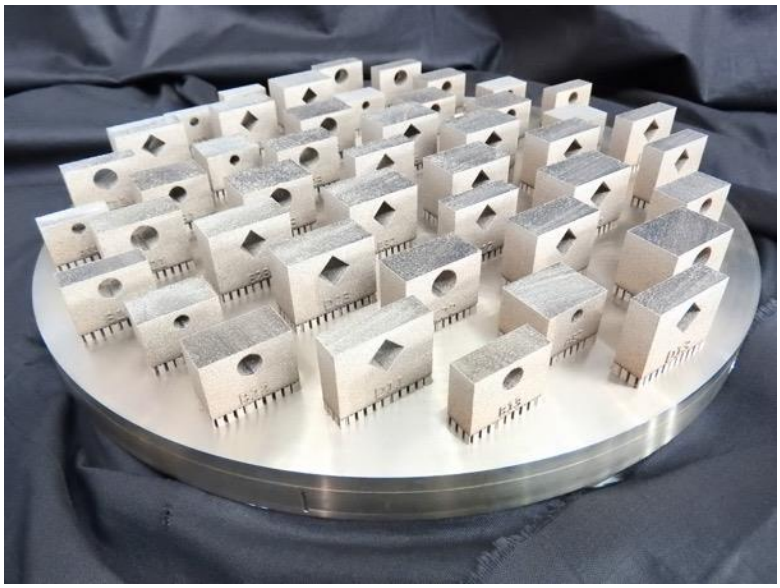

Figure 7. Produced samples with internal channels on the build plate. Build plate diameter is ø300 mm.

4.2.1 Deformation amplitude

Figure 8 depicts the numerical values of the geometrical deviations. It can be noticed that the circular channels are characterized by much larger deflections compared to the diamond shaped ones.
Concerning the circular channels, the overall results indicate that the majority of the specimens showed a negative deflection, *i.e.* the channels tend to reduce in size. Moreover, the replicates of each condition seem to show a good repeatability as the difference between them appears to be due only to the slight differences of roughness profiles. The only exceptions in these terms have to be made for the samples with a large channel diameter and large thickness, which show a profile close to the nominal one. The profiles show a visible trend of gradual increase in the deviation from the nominal profile which reaches its maximum value at the apex of the channel. Also, looking at the overall results, the deviation seems to be reduced as the diameter and the thickness of the sample increase. The deviations are significantly large going up to 0.5 mm from the nominal one.
Concerning the diamond shaped channels, it can be seen that the channel profile is similar to the nominal one. Moreover, the measurements in Figure 8 show very small geometrical deviation amplitudes. Such differences can be attributed to the particle size of the powder sintered on the walls rather than significant geometrical deviations. The analysis in terms of average deviation was conducted considering as factor also the wall (left or right) since differently from what was done for the circular channels, in this case the parameter that quantifies the deformation was measured separately for the two walls. From the individual value plot, an apparent trend of deviation function of the specimen's thickness is visible for 45° samples,

while the specimens printed at 50° inclination show no clear trend. Although a change of 5° may appear small, over the height of the diamond shaped channels it results in an extension of approximately 2 mm on the overall channel width. This results in a larger overhang regions per each layer, which can contribute to larger deformations with 45°. It should be noted that as the average differences in this case are small and should be interpreted more cautiously as deviations resultant from the internal stresses.

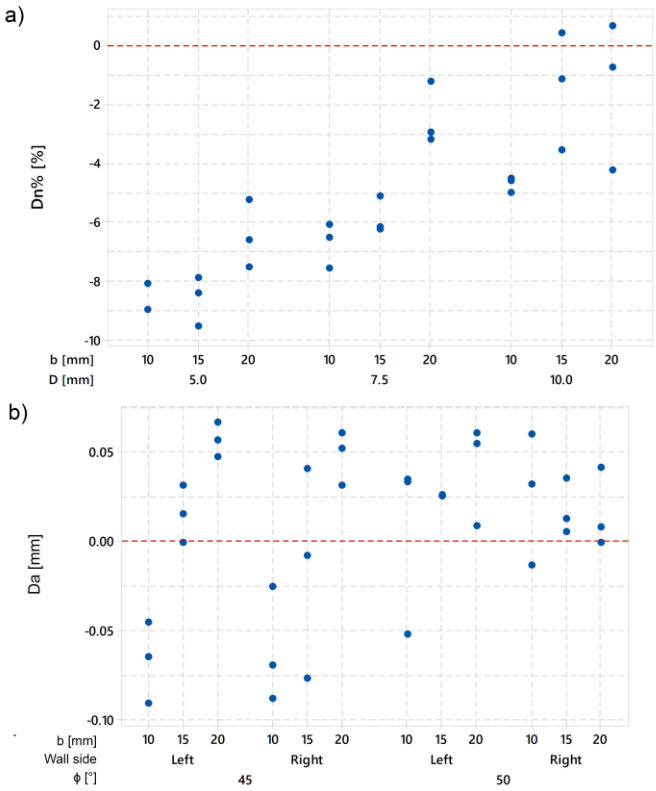

Figure 8. Individual value plot for a) the normalized deviation analysis of the circular channels, b) the average deviation from the nominal profile of the diamond shaped channels. The dashed lines indicate no deformation conditions.

These considerations confirm that the deformation behaviour of 18Ni300 is significantly different from other conventional alloys used in LPBF namely AISI 316L [9], 17-PH [13], and IN718 [45]. Overall, the circular channels appear to reduce in diameter, which can be attributed to the difference in the sign of the equivalent stress being in compression rather than traction. The fact that the final profile is clearly deformed towards the bottom is attributed to the combined effect of the thermal deformation known from literature and to the phase transformation influence that causes an expansion of the layer. Concerning the diamond shaped channels, the deformation is close to null contrarily to what has been previously observed on 17-4 PH [13]. Such result indicates almost a self-compensating behaviour where the conventionally expected tension state is balanced by a compression field.

4.2.2 Powder bed images

Figure 9 shows the powder bed at the end of the laser scan at a build height of 19.95 mm (479th layer) and 21.95 mm (519th layer) respectively above the support structures. At the 479th layer the closure of circular channels with 10 mm diameter is visible, while at the 519th layer the diamond shaped channels are near closure. The images of the powder bed monitoring system showed uncoated material protruding

from the powder bed. This can be interpreted as the majority of the specimens showing an upward deformation. Such deformation is coherent with what is previously observed for other LPBF materials. As seen in Figure 9.a, the circular channels with the largest thicknesses resulted in the most visible deformations, and also visible for the highest number of layers. In other images not reported here for the sake of brevity, the circular channel specimens with the smaller diameters showed a visible deformation only at the very last layers before the channel closure. Similarly, the diamond shaped channels depicted a visible deformation with the same trend viewed for the circular ones. These results confirm the occurrence of the thermal deformation during the process even if not measurable at the end of the process.

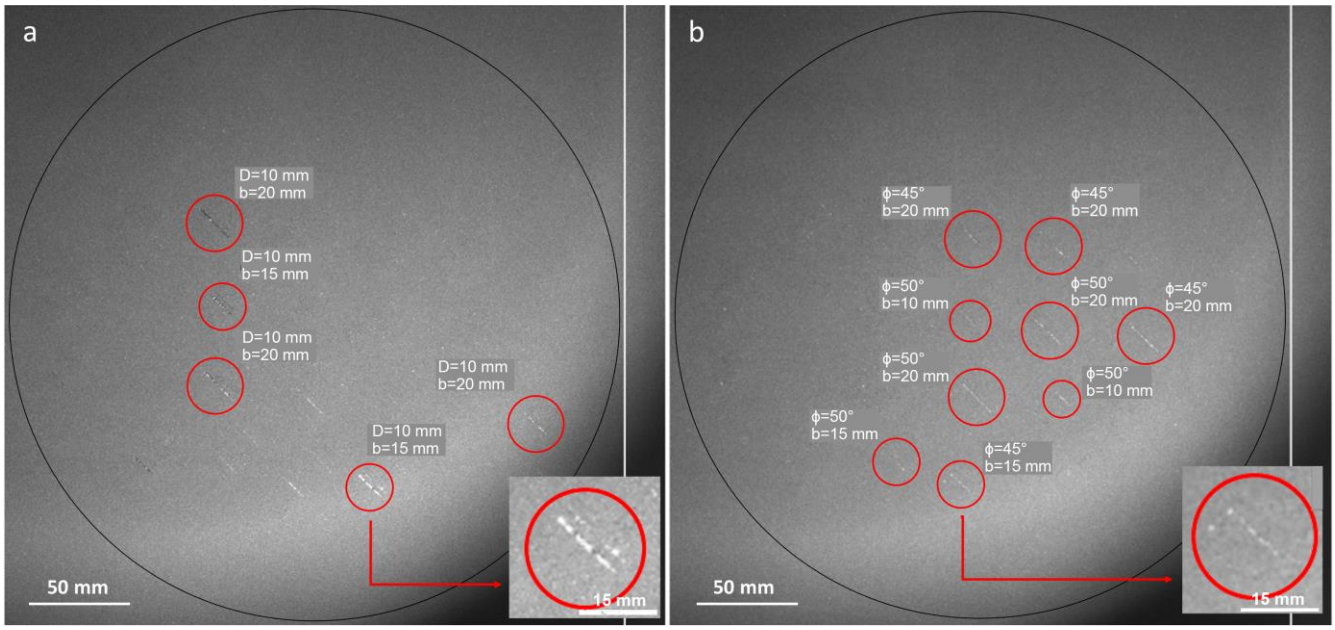

Figure 9. Powder bed monitoring after the coating of a) the 479th layer showing circular channels, and b) the 529th layer showing the diamond shaped channels. Insets show the magnified images of the protruding regions

The presence of parts protruding from the powder bed can cause the damage of the coating system as discussed in the introduction, and it is interesting to notice that this phenomenon affects also 18Ni300 maraging steels. While the upward deformation based on a tensile stress field is confirmed during the process, the final result of the downward deformation points to a physical phenomenon occurring after the closure of the internal channel.

4.2.3 Microstructure along the channel borders

One of the aspects that can be influenced by the geometry of the channel is the cooling rate in the overhanging part. For this reason, the microstructure of the material close to the channel borders was analysed, looking for any difference in terms of grain size. The grain size is compared for two specimens of different channel dimeter with 5 mm and 10 mm diameters. The grain structure was acquired at an equivalent location towards the final layers. Figure 10 shows the optical microscopy images near the channels and in the material bulk. The microstructure seems affected by the cooling conditions generated by the geometry itself causing a coarsening of the grains in the vicinity of the channel. This is expected to be due to the lower cooling rate, as expected by the fact that the overhanging part is scanned on loose powder which reduces the heat exchange. Considering the sensitivity of the 18Ni300 maraging steel to heat input, the final microstructure can be expected to be formed during the successive layers being fused on top of the channel.

It is known that during the phase transformation of steels a significant volume expansion can occur. The austenite to martensite transformation can generate a volumetric expansion up to 4% [50]. Within this work, such transformation is expected to occur around the channel borders, due to a change in the local cooling rates. The channel borders of the downfacing arch extend on the powder bed. These are the regions characterized by lower heat conductivity and heat accumulation, which can result in closure for smaller channels (D≤2 mm) [51]. In the case of 18Ni300, the heat build-up is expected to cause the volumetric expansion by phase transformation Hence, the channel geometry deviates with a negative sign with the formation of a compressive stress field.

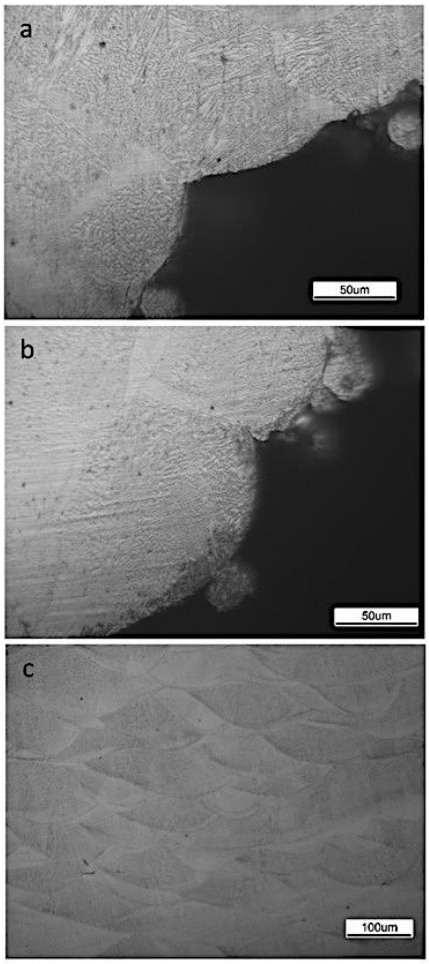

Figure 10. Microstructure of the circular channel specimens observed around the channel border of a specimen with a) 5mm, and b) 10mm diameter. c) The microstructure of the bulk material.

5 Phenomenological model of the deformation mechanism

The results allowed the formulation of a phenomenological model which describes the deformation occurring during the process as shown in Figure 11.

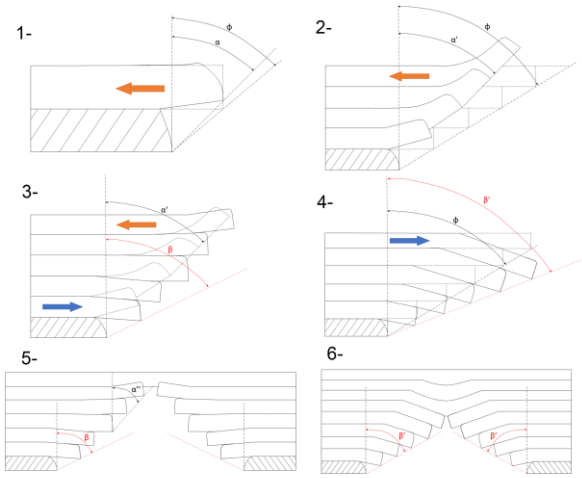

Figure 11. Schematic description of the deformation mechanism of horizontal channels during the LPBF of 18Ni300 maraging steel.

The first phenomenon acting on the layer in overhang is the shrinkage of it in the first phase of the cooling (stage 1 in Figure 11). The thermal deformation of each single layer happening in the initial cooling phase causes an upward bending which increases the angle from the nominal profile design ($\phi \rightarrow \alpha$, stage 2 in Figure 11 and Figure 9). Until this stage the deformation behaviour is similar to other conventional LPBF processed alloys such as AISI 316L [10]. Going on with the build, the accumulation of the subsequent warpage of the added layers causes the further increase of the deformation ($\alpha \rightarrow \alpha'$, stage 3 in Figure 11). At a certain point during the process the phase transformation inverts the trend of deflection induced by the shrinkage of each layer. This inversion occurs later on during the process, and starts in a region lower than the one being fused (stage 4 in Figure 11). The rescanning and remelting of the layers below the one being scanned is expected to cause phase transformation in a cyclic manner for the already deposited layer may experience multiple heating and cooling cycles. The martensitic phase transformation will occur in the layers below the one being scanned where the temperature is higher than approximately 220°C, finishing below approximately at 90° [40]. The phase transformation can start once the layers are allowed to cool down below 220°C, this happens when the part gets below the remelting region. The heating and cooling cycles are expected to proceed and progress through the layers. At this point the expansion of the successive layers, as well as an increased fraction of martensite in the previously deposited ones will cause the downward bending of the overhanging region. Finally, when the channel is closed the last layers scanned are not affected by the matrix expansion. Consequently, an upward deviation is expected for the ending part of the channel at this stage (stage 5 in Figure 11). Once the layers above the top of the channel are scanned these can transform and the expansion generates the final deformed shape visible at the end of the process (stage 6 in Figure 11). According to this model the deformation happens as a consequence of two mechanisms which occur at different times because of the delay generated by the remelting.

6 Estimation of the equivalent stress generated during LPBF

An analytical model based on that presented by Kamat and Pei [13] was used to estimate the deformation equivalent stresses generated by the end of the process. This model assumes that as a new layer is added it shrinks during the cooling generating a stress equal to the yield stress of the material being processed and the channel growing in overhang behaves according to Euler-Bernoulli's theory. Consequently, each

added layer causes a deformation of the layers below. For the sake of completeness, some of the passages required for the model development are also reported here.
The bending of each point along the profile is calculated as the result of the bending of a beam having thickness *h(x) in* Figure 12, which is the distance between the layer being added and the point of which the deformation is being calculated. Therefore, the cantilever thickness varies during the job as the layers are added and depends on the point of which the deformation is being calculated.

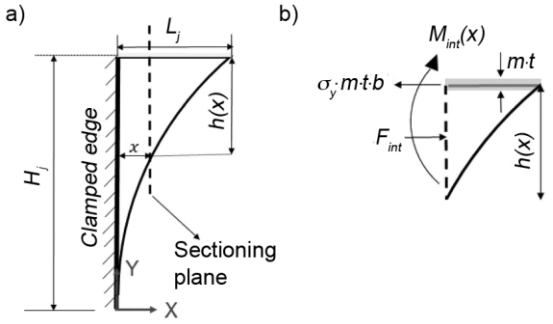

Figure 12. Schematic description of the model geometrical assumptions: a) overhang geometry and b) free-body diagram (adapted from Kamat and Pei [13]).

In Figure 12.a, H_j is the height of the part when layer j is added, L_j is the length of the j^{th} layer being added, F_{int} and M_{int} are the resulting internal force and bending moment. Considering that the melt pool penetrates more than one layer, coefficient m defined as the ratio between melt pool depth and layer thickness is introduced to consider the fact that the material involved in the shrinkage is more than the single layer. Kamat and Pei proposed an m factor of 5.17, which has also been used in work [13]. Looking at the free-body diagram shown in Figure 12.b and considering a width of the channel b, the internal force F_{int} and bending moment M_{int} generated are:

$$F_{int} = \sigma_y \cdot m \cdot t \cdot b \qquad 3$$

$$M_{int}(x) = \sigma_y \cdot m \cdot t \cdot b \, \frac{h(x) + t}{2} \qquad 4$$

where t is the layer thickness. Considering these actions, the deformation happens as the result of axial compression and bending. The axial compression according to Euler-Bernulli's beam theory for a cantilever with variable cross-sectional area A and Young modulus E is given by:

$$\delta(x) = -\frac{F_{int}}{E} \int_0^x \frac{dx}{A(x)} \qquad 5$$

Considering that the area is expressed as $A(x) = b(h(x) + t)$ the resulting compression is:

$$\delta(x) = -\frac{\sigma_y \cdot m \cdot t}{E} \int_0^x \frac{dx}{h(x) + t} \qquad 6$$

Where $\delta(x)$ is the axial deformation as a function of x. The bending induced by the momentum instead is given by the momentum-curvature relationship:

$$\frac{M_{int}(x)}{EI(x)} = \frac{d^2\Delta}{dx^2} \quad 7$$

Where Δ is the vertical deformation as a function of x.
Substituting the equation of the moment of inertia of a rectangular cross-section, $I(x) = \frac{1}{12} b[h(x) + t]^3$ the resulting equation is:

$$\frac{d^2\Delta}{dx^2} = \frac{6 \cdot \sigma_y \cdot m \cdot t}{E} \frac{1}{[h(x) + t]^2} \quad 8$$

Finally, the initial conditions to solve this second-order ordinary differential equation are:

$$\Delta = 0 \; at \; x = 0 \quad 9$$

$$\frac{d\Delta}{dx} = 0 \; at \; x = 0 \quad 10$$

considering that the beam is assumed to be clamped at one end.
These equations calculated the deformation induced by the melting of a new layer on the part below. To calculate the effect of each layer on the ones below, the overhang geometry is discretized attributing one node to the bottom corner of the overhanging part of each layer (see Figure 13). The deformation of the i^{th} layer under the action of the addition of the j^{th} layer is computed solving the equations above considering the discretization of the profile:

$$w_{ij} = \delta(x_i) = -\frac{\sigma_y \cdot m \cdot t}{E} \int_0^{x_i} \frac{dx}{h(x) + t} \quad 11$$

$$v_{ij} = \Delta(x_i) \quad 12$$

where w_{ij} and v_{ij} are the deformation of the i^{th} node induced by the j^{th} layer in x and y direction respectively. Then the deformation of each node is computed as the sum of all the deformations induced by the melting of the layer and of the ones above it.

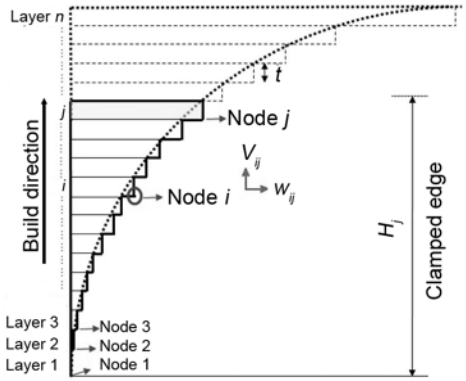

Figure 13. Nodes of the model according to the layer discretization of the geometry (adapted from Kamat and Pei [13]).

In this way the deformation of each layer is computed as:

$$w_i = \sum_{j=i}^{n} w_{ij} \quad (13)$$

$$v_i = \sum_{j=i}^{n} v_{ij} \quad (14)$$

where, w_i and v_i are the total deformation of the i^{th} node in x and y direction respectively, and n is the total number of nodes of the profile. The final profile can be computed as the sum of the deformation and the initial coordinates of the node:

$$x_i^{def} = x_i + w_i \quad (15)$$

$$y_i^{def} = y_i + v_i \quad (16)$$

where, x_i^{def} and y_i^{def} are the resulting coordinates of node i in x and y direction respectively. Since the profiles in this work are symmetric, the calculations can be made on just one half and then mirrored.
In this work the model was used inversely to estimate the equivalent stress acting on the layer starting from the resulting profile of the channel. The model was utilized iteratively varying the stress value, usually considered equal to the yield strength of the material, and the equivalent stress value is the one minimizing the total sum of squares of the difference between the predicted profile and the measured one calculated in radial direction. The equivalent stress is calculated according to the following equation:

$$\hat{\sigma}_y = \sigma_y \; that \;\; min = \sum_{k=1}^{2n} (R(\theta_i)^{pred} - R(\theta_i)^{measured})^2 \quad (17)$$

where, $\hat{\sigma}_y$ is the equivalent stress calculated by the model, $R(\theta_i)^{pred}$ is the radius predicted at the model at the angle θ_i of node i, and $R(\theta_i)^{measured}$ is the radius of the actual profile measured at the angle θ_i; the sum of the squares of the errors is calculated on the overall profile since the specimens can have asymmetry. The average elastic modulus of the as-built specimens was used in the calculations.
It should be noted that several assumptions are present in order to keep a simple closed analytical solution. The model neglects the temperature-dependent material properties. Such assumption provides ease of calculation although this may cause inaccuracy especially for the Young's modulus. The plastic deformation is also not included in the model. Such condition would also improve the fidelity of the model for estimating the deformation behaviour starting from the known model variables. The volumetric expansion, which is also not described in the current form, could be incorporated as a geometrical change to further improve the model. Incorporating a thermal model that is able to incorporate the heat build-up and changes in the cooling rates due to the part geometry would be of great benefit. Coupled thermo-mechanical simulations can be a more appropriate method for such objective [32]. It is underlined that the model was employed in this work as a means to calculate the equivalent stress field at the end of the build process, in order to better define the observed phenomenon.
The diamond shaped channels were much closed to the nominal profile in the overall experimented conditions. This can be interpreted as the equivalent stress field is approximately null. Hence, only the circular profiles measured were analysed. The main effect and interaction plots of the equivalent stress measurements are reported in Figure 14. The results are coherent with the deformation analysis

concerning the overall trend. The negative sign shows that the material is under compression in the majority of the tested conditions. Moreover, deeper channels and larger diameters appear to provide the means to reduce the compression field. The estimated stress fields for the smallest channel diameters and shallower channels also exceed the material's yield strength in as-built conditions with the tensile specimens. While this can be interpreted as the formation of permanent deformations, it can also indicate the variation of material properties in the vicinity of the channel profile. The strong variation between the different channel sizes indicate the influence of the channel geometry on the heating and cooling cycles. The shape of the channel determines the size of the scan path profile as well as the underlying mass that will dissipate the heat during the process. The smaller channels are expected to the cause a larger heat accumulation due to the shorter scan vectors resulting in a shorter temporal distance between the overlapping hatch lines [52]. Moreover the smaller surface area of the channels with smaller diameters can reduce the thermal conduction to the powder bed. With these combined effects, the phase transformation is expected to be more pronounced resulting in larger fraction of martensitic transformation around the channels. Hence the overlapping layers with larger fraction of martensite are expected to compress further into the channel. Resultantly, the larger geometrical errors are formed corresponding to a larger equivalent stress field.

The equivalent stresses obtained with this model were also analysed with analysis of variance (ANOVA) with a statistical significance threshold of α=5%. The results shown in Table 6 confirmed the significative influence of both the geometrical parameters and the non-significance of their interaction.

In the light of all the results, it can be seen that the deformation behaviour of 18Ni300 is geometry dependant. It can be inferred that the thermal history, shrinkage and the phase transformation may have a great influence on the stress distribution.

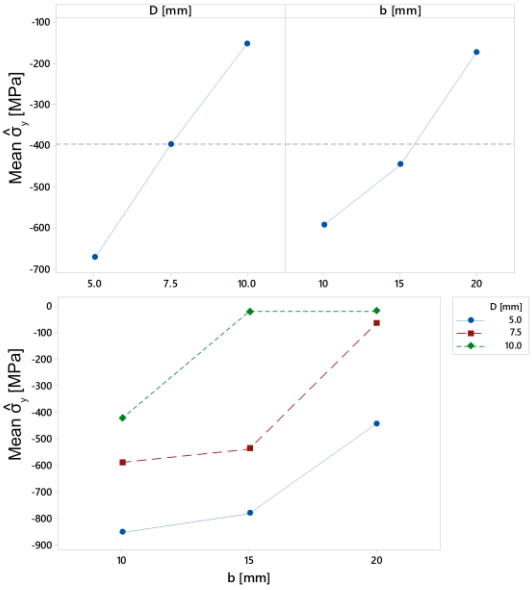

Figure 14. Main effects and interaction plots of the equivalent stresses estimates.

Although the analysis confirms the change in the stress field behaviour to better explain the unusual deformation behaviour of 18Ni300 horizontal channels processed by LPBF, the model validation remains an open issue. The measurement of stress fields is highly complex on the as-built specimens due to the high surface roughness, which would be problematic for X-ray diffraction (XRD) measurements. Surface polishing and grinding would cause material removal and consequently a change in the stress field. Such principle can be exploited for measurements via stress gauges while the part is released via chip removal or wire electric discharge machining [11]. However, the measurement of the local stress field remains

problematic due to the size restrictions. In-situ measurements have been also discussed in literature, which can better shed light on this phenomenon [53,54].

Table 6. Analysis of variance on the equivalent stress.

Source	DF	Adj SS	Adj MS	F-Value	P-Value
D [mm]	2	1210196	605098	17.44	0.000
b [mm]	2	860066	430033	12.39	0.000
D [mm]*b [mm]	4	202438	50610	1.46	0.258
Error	17	589931	34702		
Total	25	2827630			

7 Conclusions

This work was aimed at studying the deformation occurring in the horizontal channels during the LPBF of 18Ni300 maraging steel for tooling applications with conformal cooling channels. The geometrical integrity of the conformal channels is fundamental for the efficient cooling having an impact both on the tool lifetime and the quality of the product quality. The systematic analysis showed several differences in the deformation behaviour compared to some of the conventional alloys used in LPBF. The main outcomes of the work can be summarized as follows:

- A suitable set of parameters for producing maraging steel 18Ni300 was defined resulting in mechanical properties compliant to the expected ones both in the as-built and in the aged conditions;
- 18Ni300 showed a peculiar behaviour of downward bending and a compressive equivalent stress, which were associated to the martensitic structure which is formed with a significative volumetric expansion. Such deformation behaviour was not observed with other conventional LPBF alloys;
- The deformation was shown to be dependent on the geometry of the channel being produced, in particular shorter and smaller channels exhibit higher amount of closure;
- For the circular channels a larger diameter resulted in a final profile close to the nominal one, while for the diamond shaped geometrical fidelity was higher;
- The powder bed monitoring images showed that an upward deformation happens during the build causing the formation of parts protruding from the powder bed;
- A phenomenological model was formulated stating that the deformation is a combination of the initial thermal deformation, which causes an upward deformation, followed by a volumetric expansion due to the phase transformation which inverts the previous trend.

In industrial practice, the channels are expected to vary also in length, diameter and orientation. Hence, the final geometrical deviations will be the result of a complex interplay between the position, dimension and the shape of the channel. Although the diamond shaped channels appear to suffer much less in terms of geometrical deviations, their use is limited due the stress accumulation expected in the sharp corners. Such conditions are problematic for thermal fatigue problems. Finally, a more comprehensive analysis can be carried out to embed the channel deformation behaviour to finite element models starting from a semi-empirical approach such as the one defined here. The end users can define compensated models and work on finishing operations for the specific case in hand.

Acknowledgements

The authors gratefully acknowledge the collaboration of Trumpf Srl. The Italian Ministry of Education, University and Research is acknowledged for the support provided through the Project "Department of Excellence LIS4.0 - Lightweight and Smart Structures for Industry 4.0”.

References

[1] Liu C, Cai Z, Dai Y, Huang N, Xu F, Lao C. Experimental comparison of the flow rate and cooling performance of internal cooling channels fabricated via selective laser melting and conventional drilling process. Int J Adv Manuf Technol 2018;96:2757–67. doi:10.1007/s00170-018-1799-y.

[2] Mazur M, Leary M, McMillan M, Elambasseril J, Brandt M. SLM additive manufacture of H13 tool steel with conformal cooling and structural lattices. Rapid Prototyp J 2016;22:504–18. doi:10.1108/RPJ-06-2014-0075.

[3] Pakkanen J, Calignano F, Trevisan F, Lorusso M, Ambrosio EP, Manfredi D, et al. Study of Internal Channel Surface Roughnesses Manufactured by Selective Laser Melting in Aluminum and Titanium Alloys. Metall Mater Trans A Phys Metall Mater Sci 2016;47:1–8. doi:10.1007/s11661-016-3478-7.

[4] Anilli M, Demir AG, Previtali B. Additive manufacturing of laser cutting nozzles by SLM: processing, finishing and functional characterization. Rapid Prototyp J 2018;24. doi:10.1108/RPJ-05-2017-0106.

[5] Lopez E, Felgueiras T, Grunert C, Brückner F, Riede M, Seidel A, et al. Evaluation of 3D-printed parts by means of high-performance computer tomography. J Laser Appl 2018;30:032307. doi:10.2351/1.5040644.

[6] Calignano F. Design optimization of supports for overhanging structures in aluminum and titanium alloys by selective laser melting. Mater Des 2014;64:203–13. doi:10.1016/j.matdes.2014.07.043.

[7] Finazzi V, Demir AG, Biffi CA, Chiastra C, Migliavacca F, Petrini L, et al. Design Rules for Producing Cardiovascular Stents by Selective Laser Melting: Geometrical Constraints and Opportunities. Procedia Struct Integr 2019;15:16–23. doi:10.1016/j.prostr.2019.07.004.

[8] Snyder JC, Stimpson CK, Thole KA, Mongillo DJ. Build Direction Effects on Microchannel Tolerance and Surface Roughness. J Mech Des 2015;137:111411. doi:10.1115/1.4031071.

[9] Wang D, Mai S, Xiao D, Yang Y. Surface quality of the curved overhanging structure manufactured from 316-L stainless steel by SLM. Int J Adv Manuf Technol 2016;86:781–92. doi:10.1007/s00170-015-8216-6.

[10] Wang D, Yang Y, Yi Z, Su X. Research on the fabricating quality optimization of the overhanging surface in SLM process. Int J Adv Manuf Technol 2013;65:1471–84. doi:10.1007/s00170-012-4271-4.

[11] Mercelis P, Kruth J-PJ. Residual stresses in selective laser sintering and selective laser melting. Rapid Prototyp J 2006;12:254–65. doi:10.1108/13552540610707013.

[12] Ali H, Ghadbeigi H, Hosseinzadeh F, Oliveira J, Mumtaz K. Effect of pre-emptive in situ parameter modification on residual stress distributions within selective laser-melted Ti6Al4V components. Int J Adv Manuf Technol 2019;103:4467–79. doi:10.1007/s00170-019-03860-6.

[13] Kamat AM, Pei Y. An analytical method to predict and compensate for residual stress-induced deformation in overhanging regions of internal channels fabricated using powder bed fusion. Addit Manuf 2019;29:100796. doi:10.1016/j.addma.2019.100796.

[14] Amphyon. No Title n.d. https://altairhyperworks.com/partner/amphyon.

[15] Simufact Additive n.d.

[16] Clijsters S, Craeghs T, Buls S, Kempen K, Kruth JP. In situ quality control of the selective laser melting process using a high-speed, real-time melt pool monitoring system. Int J Adv Manuf Technol 2014;75:1089–101. doi:10.1007/s00170-014-6214-8.

[17] Vasileska E, Demir AG, Colosimo BM, Previtali B. Layer-wise control of selective laser melting by means of inline melt pool area measurements. J Laser Appl 2020;32:022057. doi:10.2351/7.0000108.

[18] Robinson JH, Ashton IRT, Jones E, Fox P, Sutcliffe C. The effect of hatch angle rotation on parts manufactured using selective laser melting. Rapid Prototyp J 2019;25:289–98. doi:10.1108/RPJ-06-2017-0111.

[19] Kruth JP, Deckers J, Yasa E, Wauthlé R. Assessing and comparing influencing factors of residual stresses in selective laser melting using a novel analysis method. Proc Inst Mech Eng Part B J Eng Manuf 2012;226:980–91. doi:10.1177/0954405412437085.

[20] Mertens R, Clijsters S, Kempen K, Kruth J-P. Optimization of Scan Strategies in Selective Laser Melting of Aluminum Parts With Downfacing Areas. J Manuf Sci Eng 2014. doi:10.1115/1.4028620.

[21] Ali H, Ghadbeigi H, Mumtaz K. Effect of scanning strategies on residual stress and mechanical properties of Selective Laser Melted Ti6Al4V. Mater Sci Eng A 2018;712:175–87. doi:10.1016/j.msea.2017.11.103.

[22] Kempen K, Vrancken B, Buls S, Thijs L, Van Humbeeck J, Kruth J-P. Selective Laser Melting of Crack-Free High Density M2 High Speed Steel Parts by Baseplate Preheating. J Manuf Sci Eng 2014;136:061026. doi:10.1115/1.4028513.

[23] Buchbinder D, Meiners W, Pirch N, Wissenbach K, Schrage J. Investigation on reducing distortion by preheating during manufacture of aluminum components using selective laser melting. J Laser Appl 2014;26:012004. doi:10.2351/1.4828755.

[24] Fayazfar H, Salarian M, Rogalsky A, Sarker D, Russo P, Paserin V, et al. A critical review of powder-based additive manufacturing of ferrous alloys: Process parameters, microstructure and mechanical properties. Mater Des 2018;144:98–128. doi:10.1016/j.matdes.2018.02.018.

[25] Averyanova M, Cicala E, Bertrand P, Grevey D. Experimental design approach to optimize selective laser melting of martensitic 17-4 PH powder: part I – single laser tracks and first layer. Rapid Prototyp J 2012;18:28–37. doi:10.1108/13552541211193476.

[26] Rafi HK, Starr TL, Stucker BE. A comparison of the tensile, fatigue, and fracture behavior of Ti-6Al-4V and 15-5 PH stainless steel parts made by selective laser melting. Int J Adv Manuf Technol 2013;69:1299–309. doi:10.1007/s00170-013-5106-7.

[27] ASM International. “Maraging Steels,” in Properties and Selection: Irons, Steels, and High-Performance Alloys, ASM Handbook. 1990.

[28] Bai Y, Yang Y, Wang D, Zhang M. Influence mechanism of parameters process and mechanical properties evolution mechanism of maraging steel 300 by selective laser melting. Mater Sci Eng A 2017;703:116–23. doi:10.1016/j.msea.2017.06.033.

[29] Ahn DG. Applications of laser assisted metal rapid tooling process to manufacture of molding & forming tools - state of the art. Int J Precis Eng Manuf 2011;12:925–38. doi:10.1007/s12541-011-0125-5.

[30] Zhang C, Wang S, Li J, Zhu Y, Peng T, Yang H. Additive manufacturing of products with functional fluid channels: A review. Addit Manuf 2020;36:101490. doi:10.1016/j.addma.2020.101490.

[31] Armillotta A, Baraggi R, Fasoli S. SLM tooling for die casting with conformal cooling channels. Int J Adv Manuf Technol 2014;71:573–83. doi:10.1007/s00170-013-5523-7.

[32] Bruna-Rosso C, Mergheim J, Previtali B. Finite element modeling of residual stress and geometrical error formations in selective laser melting of metals. Proc Inst Mech Eng Part C J Mech Eng Sci 2020;235:2022–38. doi:10.1177/0954406220943225.

[33] Becker TH, DImitrov Di. The achievable mechanical properties of SLM produced Maraging Steel 300 components. Rapid Prototyp J 2016;22:487–94. doi:10.1108/RPJ-08-2014-0096.

[34] Suryawanshi J, Prashanth KG, Ramamurty U. Tensile, fracture, and fatigue crack growth properties of a 3D printed maraging steel through selective laser melting. J Alloys Compd 2017;725:355–64. doi:10.1016/j.jallcom.2017.07.177.

[35] Tan C, Zhou K, Ma W, Zhang P, Liu M, Kuang T. Microstructural evolution, nanoprecipitation behavior and mechanical properties of selective laser melted high-performance grade 300 maraging steel. Mater Des 2017;134:23–34. doi:10.1016/j.matdes.2017.08.026.

[36] Demir AG, Colombo P, Previtali B. From pulsed to continuous wave emission in SLM with contemporary fiber laser sources: effect of temporal and spatial pulse overlap in part quality. Int J Adv Manuf Technol 2017;91. doi:10.1007/s00170-016-9948-7.

[37] Demir AG, De Giorgi C, Previtali B. Design and Implementation of a Multisensor Coaxial Monitoring System with Correction Strategies for Selective Laser Melting of a Maraging Steel. J Manuf Sci Eng Trans ASME 2018;140. doi:10.1115/1.4038568.

[38] Mutua J, Nakata S, Onda T, Chen ZC. Optimization of selective laser melting parameters and influence of post heat treatment on microstructure and mechanical properties of maraging steel. Mater Des 2018;139:486–97. doi:10.1016/j.matdes.2017.11.042.

[39] Monkova K, Zetkova I, Kučerová L, Zetek M, Monka P, Daňa M. Study of 3D printing direction and effects of heat treatment on mechanical properties of MS1 maraging steel. Arch Appl Mech 2019;89:791–804. doi:10.1007/s00419-018-1389-3.

[40] Casati R, Lemke JN, Tuissi A, Vedani M. Aging behaviour and mechanical performance of 18-Ni 300 steel processed by selective laser melting. Metals (Basel) 2016;6. doi:10.3390/met6090218.

[41] Bhardwaj T, Shukla M. Effect of laser scanning strategies on texture, physical and mechanical properties of laser sintered maraging steel. Mater Sci Eng A 2018;734:102–9. doi:10.1016/j.msea.2018.07.089.

[42] Demir AG, Previtali B. Investigation of remelting and preheating in SLM of 18Ni300 maraging steel as corrective and preventive measures for porosity reduction. Int J Adv Manuf Technol 2017;93:1–13. doi:10.1007/s00170-017-0697-z.

[43] Tan C, Zhou K, Kuang M, Ma W, Kuang T. Microstructural characterization and properties of selective laser melted maraging steel with different build directions. Sci Technol Adv Mater 2018;19:746–58. doi:10.1080/14686996.2018.1527645.

[44] Jägle EA, Choi PP, Van Humbeeck J, Raabe D. Precipitation and austenite reversion behavior of a maraging steel produced by selective laser melting. J Mater Res 2014;29:2072–9. doi:10.1557/jmr.2014.204.

[45] Wildgoose AJ, Thole KA, Sanders P, Wang L. Impact of Additive Manufacturing on Internal Cooling Channels with Varying Diameters and Build Directions. ASME Turbo Expo 2020 Turbomach Tech Conf Expo 2020.

[46] Zhang X, Kang J, Rong Y, Wu P, Feng T. Effect of scanning routes on the stress and deformation of overhang structures fabricated by SLM. Materials (Basel) 2018;12. doi:10.3390/ma12010047.

[47] Bugatti M, Semeraro Q. Limitations of the inherent strain method in simulating powder bed fusion processes. Addit Manuf 2018;23:329–46. doi:10.1016/j.addma.2018.05.041.

[48] Caprio L, Demir AG, Previtali B. Influence of pulsed and continuous wave emission on melting efficiency in selective laser melting. J Mater Process Tech 2019;266:429–41. doi:10.1016/j.jmatprotec.2018.11.019.

[49] Caprio L, Demir AG, Previtali B. Comparative study between CW and PW emissions in selective laser melting. J Laser Appl 2018;30. doi:10.2351/1.5040631.

[50] den Ouden G, Hermans M. Welding Technology. VSSD Delft; 2009.

[51] Solyaev Y, Rabinskiy L, Tokmakov D. Overmelting and closing of thin horizontal channels in AlSi10Mg samples obtained by selective laser melting. Addit Manuf 2019;30:100847. doi:10.1016/j.addma.2019.100847.

[52] Vasileska E, Demir AG, Colosimo BM, Previtali B. Layer-wise control of selective laser melting

by means of inline melt pool area measurements. Proc. ICALEO 2019, 2019, p. 1–11.

[53] Schmeiser F, Krohmer E, Schell N, Uhlmann E, Reimers W. Experimental obserSchmeiser, F., Krohmer, E., Schell, N., Uhlmann, E., Reimers, W., 2020. Experimental observation of stress formation during selective laser melting using in situ X-ray diffraction. Addit. Manuf. 32, 101028. doi:10.1016/j.addma.2019.10102. Addit Manuf 2020;32:101028. doi:10.1016/j.addma.2019.101028.

[54] Wen Y, Zhang B, Liu S, Cai W, Wang P, Lee CJJ, et al. A novel experimental method for in situ strain measurement during selective laser melting. Virtual Phys Prototyp 2020;15:583–95. doi:10.1080/17452759.2020.1842137.